Atomic-Scale Chemical Imaging of Composition and Bonding by Aberration-Corrected Microscopy

D. A. Muller, *et al.*
Science **319**, 1073 (2008);
DOI: 10.1126/science.1148820

nacre and other biological materials (Fig. 3C). The elastic moduli of up to 10 GPa achieved by the artificial composite is comparable to those of dentin and bone (9, 28, 29) and about 10-fold lower than that of nacre (7).

The use of high-strength artificial platelets as mechanical reinforcement imposes less-stringent microstructural requirements to the composites in comparison to natural hybrid structures. Artificial composites reinforced with strong platelets show remarkable mechanical properties in spite of their less-elaborate microstructure. In contrast, the relatively weak inorganic compounds available in nature for biomineralization require a far more sophisticated architecture to render materials with comparable mechanical behavior. Nature still remains supreme in its ability to build hybrid materials with unique structures and properties using a relatively limited variety of inorganic building blocks. Further advances in this area might allow us to replicate the microstructure of natural materials by using strong artificial building blocks in the future. If successful, this bio-inspired approach would eventually lead to man-made hybrid materials with unprecedented mechanical properties.

References and Notes

1. H. A. Lowenstam, S. Weiner, *On Biomineralization* (Oxford Univ. Press, New York, 1989), pp. 336.
2. R. Z. Wang, Z. Suo, A. G. Evans, N. Yao, I. A. Aksay, *J. Mater. Res.* **16**, 2485 (2001).
3. H. J. Gao, B. H. Ji, I. L. Jager, E. Arzt, P. Fratzl, *Proc. Natl. Acad. Sci. U.S.A.* **100**, 5597 (2003).
4. G. Mayer, *Science* **310**, 1144 (2005).
5. N. Nassif et al., *Proc. Natl. Acad. Sci. U.S.A.* **102**, 12653 (2005).
6. J. D. Currey, *Proc. R. Soc. London Ser. B* **196**, 443 (1977).
7. A. P. Jackson, J. F. V. Vincent, R. M. Turner, *Proc. R. Soc. London Ser. B* **234**, 415 (1988).
8. H. D. Wagner, S. Weiner, *J. Biomech.* **25**, 1311 (1992).
9. I. Jager, P. Fratzl, *Biophys. J.* **79**, 1737 (2000).
10. A. G. Evans et al., *J. Mater. Res.* **16**, 2475 (2001).
11. F. Barthelat, H. Tang, P. D. Zavattieri, C. M. Li, H. D. Espinosa, *J. Mech. Phys. Solids* **55**, 306 (2007).
12. J. Rexer, E. Anderson, *Polym. Eng. Sci.* **19**, 1 (1979).
13. E. R. Kleinfeld, G. S. Ferguson, *Science* **265**, 370 (1994).
14. Z. Y. Tang, N. A. Kotov, S. Magonov, B. Ozturk, *Nat. Mater.* **2**, 413 (2003).
15. I. Chasiotis, Q. Chen, G. M. Odegard, T. S. Gates, *Exp. Mech.* **45**, 507 (2005).
16. P. B. Messersmith, E. P. Giannelis, *Chem. Mater.* **6**, 1719 (1994).
17. D. Schmidt, D. Shah, E. P. Giannelis, *Curr. Opin. Solid State Mater. Sci.* **6**, 205 (2002).
18. P. Podsiadlo et al., *Science* **318**, 80 (2007).
19. N. Sheng et al., *Polymers* **45**, 487 (2004).
20. A. Okada, A. Usuki, *Mater. Sci. Eng. C* **3**, 109 (1995).
21. B. Glavinchevski, M. Piggott, *J. Mater. Sci.* **8**, 1373 (1973).
22. D. Hull, T. W. Clyne, *An Introduction to Composite Materials*, D. R. Clark, S. Suresh, I. M. Ward, Eds., Cambridge Solid State Science Series (Cambridge Univ. Press, Cambridge, ed. 2, 1996).
23. D. G. H. Ballard, G. R. Rideal, *J. Mater. Sci.* **18**, 545 (1983).
24. N. Almqvist et al., *Mater. Sci. Eng. C* **7**, 37 (1999).
25. Materials and methods are available on *Science* Online.
26. H. L. Cox, *Br. J. Appl. Phys.* **3**, 72 (1952).
27. G. E. Padawer, N. Beecher, *Polym. Eng. Sci.* **10**, 185 (1970).
28. H. Sano, B. Ciucchi, W. G. Matthews, D. H. Pashley, *J. Dent. Res.* **73**, 1205 (1994).
29. W. J. Landis, J. J. Librizzi, M. G. Dunn, F. H. Silver, *J. Bone Miner. Res.* **10**, 859 (1995).
30. We thank V. Klass, I. Olliges, and C. Müller for their contribution to the experimental part of this study and ETH Zurich for financial support.

Atomic-Scale Chemical Imaging of Composition and Bonding by Aberration-Corrected Microscopy

D. A. Muller,[1,2]* L. Fitting Kourkoutis,[1] M. Murfitt,[3] J. H. Song,[4,5] H. Y. Hwang,[5,6] J. Silcox,[1,2] N. Dellby,[3] O. L. Krivanek[3]

Using a fifth-order aberration-corrected scanning transmission electron microscope, which provides a factor of 100 increase in signal over an uncorrected instrument, we demonstrated two-dimensional elemental and valence-sensitive imaging at atomic resolution by means of electron energy-loss spectroscopy, with acquisition times of well under a minute (for a 4096-pixel image). Applying this method to the study of a $La_{0.7}Sr_{0.3}MnO_3/SrTiO_3$ multilayer, we found an asymmetry between the chemical intermixing on the manganese-titanium and lanthanum-strontium sublattices. The measured changes in the titanium bonding as the local environment changed allowed us to distinguish chemical interdiffusion from imaging artifacts.

Resolving and identifying the composition and bonding of all atoms in a solid sample at atomic resolution has been a long-standing goal of analytical microscopy. Atom probe microscopy comes close to the first goal of compositional identification, collecting roughly 60% of the atoms field-evaporated off a sharp tip and locating their positions to within a few lattice sites. Electron energy-loss spectroscopy (EELS) of a high-energy electron beam focused down to atomic dimensions allows elemental identification with atomic resolution, with the additional capabilities of imaging insulating materials and determining the electronic structure or chemical bonding of each atomic column in the material (1).

One step toward atomic-resolution EELS imaging was the identification of the chemical state at a single point at an interface, with the use of a scanning transmission electron microscope (STEM) (2). However, the resolution was limited by a small incident electron beam current, allowing bonding states to be mapped at subnanometer but not atomic resolution (3). The recent correction of third-order electron-optical aberrations by multipole correctors has allowed the illumination aperture size to be increased, yielding a factor of 4 to 6 increase in the beam current for the same probe size (4). This has made it possible to record atomic-resolution EELS line profiles (5) or chemical images without bonding information (6, 7).

A full two-dimensional chemical map obtained by EELS that also contains bonding information requires yet another order of magnitude increase in the beam current to improve the signal-to-noise ratio. We did so by correcting the electron optical aberrations to fifth-order so the numerical aperture in the STEM could be further increased (8). However, even this increase in beam current was not sufficient to produce a true chemical map. Electrons are scattered both elastically and inelastically in the sample. Although the inelastic scattering that contains the EELS signal is peaked largely in the forward direction, the unavoidable elastic scattering of those same electrons is strongly angle-dependent. Standard collection optics capture only a portion of the inelastically scattered electrons, because heavier atoms elastically scatter them out of the path to the detector. Consequently, the EELS signal can be dominated by changes in the elastic contrast, masking the chemically unique inelastic signal.
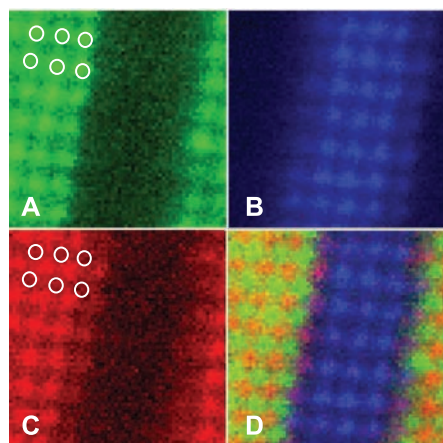
This phenomenon was recently demonstrated, both by experiment and quantitative theory, for $Bi_{0.5}Sr_{0.5}MnO_3$, where the "inelastic" images were dominated by the strong elastic scattering from the Bi sites that largely prevented electrons on the Bi column from entering the detector (6). A general symptom of this scattering artifact is that all inelastic intensities, independent of their characteristic energy loss, would peak at the same spatial locations [as was mentioned in (9)]. The artifact can be eliminated if all the elastically scattered electrons are being collected by the spectrometer. However, increasing the collection angle of a conventional spectrometer to do this is not possible without drastically degrading the

[1]Applied and Engineering Physics, Cornell University, Ithaca, NY 14853, USA. [2]Kavli Institute at Cornell, Cornell University, Ithaca, NY 14853, USA. [3]Nion Co., Kirkland, WA 98033, USA. [4]Department of Physics, Chungnam National University, Daejeon 305-764, Korea. [5]Department of Advanced Materials Science, University of Tokyo, Kashiwa, Chiba 277-8561, Japan. [6]Japan Science and Technology Agency, Kawaguchi 332-0012, Japan.

*To whom correspondence should be addressed. E-mail: dm24@cornell.edu

energy resolution to the point that the EELS edges are no longer detectable (*10*). By adding four round coupling lenses that parallelize the scattered electrons, plus a corrective quadrupole/octupole module before the spectrometer (*8*), we obtained 0.5-eV energy resolution for collection angles as large as 60 mrad. These angles are larger than those in a conventional system by a factor of roughly 3 to 6, and they collect a much larger fraction of the elastically scattered energy-loss electrons and thereby reduce the measured elastic modulation to below a few percent.

Figure 1 shows atomic-resolution EELS maps that demonstrate this capability. The underlying spectrum image was recorded with an incident beam current of ~780 pA, with ~600 pA collected in the spectrometer (*11*). For comparison, the reported incident beam currents of third-order correctors range from 10 to 100 pA when used for EELS mapping, with an estimated usable EELS signal of 8 to 50 pA (*11*). This factor of 10 to 100 increase in signal can be attributed to a high-brightness source, improved probe formation, and efficient signal collection. An uncorrected microscope has a probe-forming aperture semi-angle of ~10 mrad. A third-order corrector allows this angle to be doubled, increasing the beam current fourfold for the same source size. A fifth-order corrector allows the angle to be doubled yet again, giving a factor of 16 increase in beam current over the uncorrected system. An additional factor of 10 in current is gained by using a cold field emitter
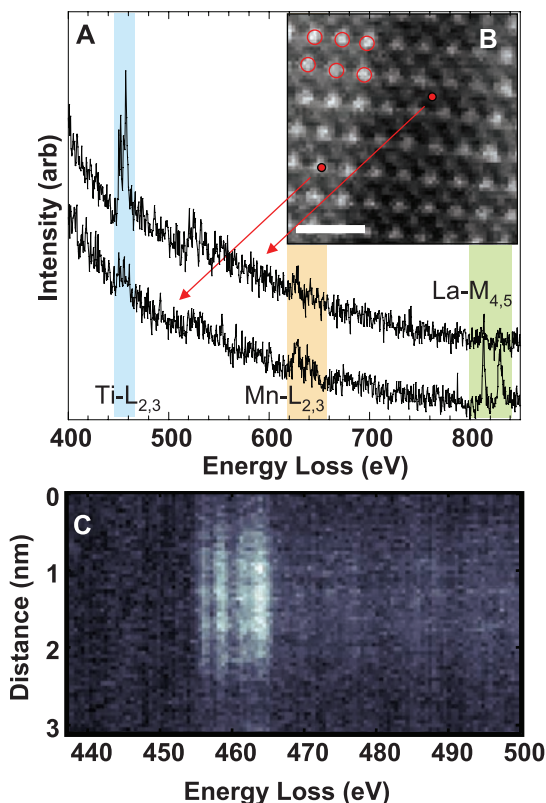
instead of the more common Schottky emitter. Finally, the post-specimen optics were matched to collect over a much wider range of scattering angles than in uncorrected instruments (*8*).

The sample we studied is a perovskite $La_{0.7}Sr_{0.3}MnO_3/SrTiO_3$ (LSMO/STO) multilayer, with five nominal unit cells of each material, grown in conditions where cation interdiffusion occurs; such a multilayer is useful for the bonding studies presented below (*11*). This sample is a good resolution test because there are two distinct sublattices, Sr-La and Mn-Ti, offset from each other by 0.19 nm, and the edges of the multilayers themselves provide a "knife-edge" resolution test where the resulting image is essentially a convolution of the probe shape with a step function. This is a useful check for probe tails that are filtered out of a periodic lattice image. Both tests are needed to distinguish between true inelastic contrast and the preservation of the elastic contrast in the inelastic channel (*12*). Here, the La and Mn lattice images are properly offset from each other (Fig. 1, A and C), showing that the elastic contrast artifact (which would cause them to coincide) has been suppressed.

Figure 2A shows some of the individual spectra that make up the chemical map, and the simultaneously recorded annular dark-field image from the elastic signal (Fig. 2B) shows that the EELS signals are properly registered with their respective atomic columns. The sharp left edge of the STO layer visible as the dark band in the center of Fig. 1A shows the abrupt profile in the La signal. Another map of a nearby region of the sample, recorded with the same probe alignments, shows

an abrupt edge profile for Ti (*11*) (fig. S2). This counterexample demonstrates that the more gradual interfaces for the Ti and Mn signals in Fig. 1, B and C, are not the result of inelastic delocalization [which will be worst for Ti, the lowest-energy edge (*13–15*)] or of probe spreading, but rather are a property of the sample itself.
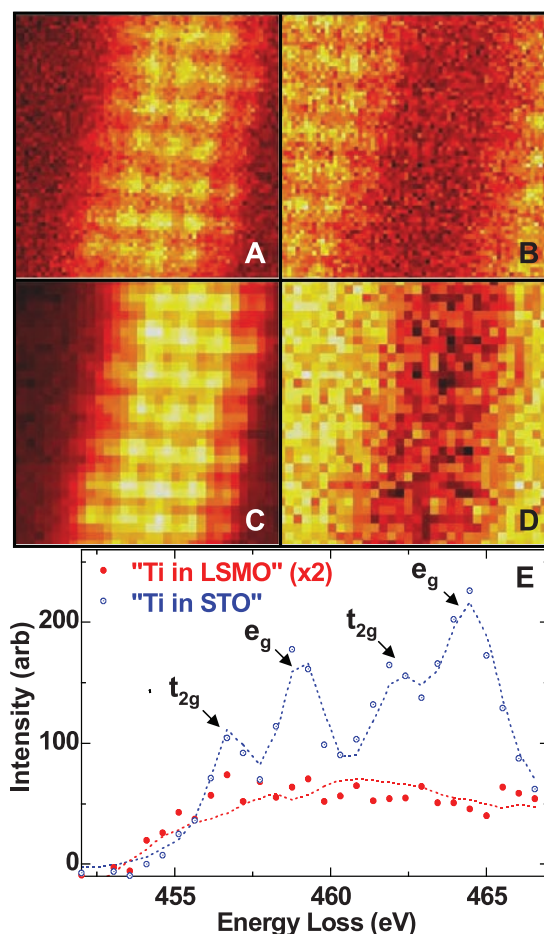
With these data we were able to explore chemical bonding states at an atomic scale. The shape of the EELS edge reflects the local, final-state density of states modified by the presence of a core hole on a specific atom column (*16*). The bonding changes are most noticeable at an energy scale of 0.2 to 2 eV, so a simple check that we have sufficient signal to image bonding states is to display maps of the EELS fine structure formed with energy windows in this range (Fig. 3, A and B, for Ti and Mn, respectively, using a 0.5-eV window). The changes in EELS fine structure are complex, but some general bonding trends are captured by a principal components analysis of the spectrum image (*17*). The component that contains the largest image variance, PC1 (Fig. 3C), tracks the average shape of the Ti L edge and follows the map of total Ti signal. We found that the second-largest component, PC2 (Fig. 3D), tracks the differences in Ti bonding between Ti-rich STO and Ti-poor LSMO layers (spectra shown in Fig. 3E). PC2 is only ~15% the intensity of PC1, so the lattice fringe modulation is reduced below the noise level in PC2. Nonetheless, the presence of PC2 allowed us to distinguish between imaging artifacts, such as the small but unavoidable probe tails due to beam spreading, and chemical interdiffusion in the sample itself. Probe tails will blur the Ti signal of PC1 spatially but

Fig. 1. Spectroscopic imaging of a $La_{0.7}Sr_{0.3}MnO_3/SrTiO_3$ multilayer, showing the different chemical sublattices in a 64 × 64 pixel spectrum image extracted from 650 eV–wide electron energy-loss spectra recorded at each pixel. (**A**) La M edge; (**B**) Ti L edge; (**C**) Mn L edge; (**D**) red-green-blue false-color image obtained by combining the rescaled Mn, La, and Ti images. Each of the primary color maps is rescaled to include all data points within two standard deviations of the image mean. Note the lines of purple at the interface in (D), which indicate Mn-Ti intermixing on the B-site sublattice. The white circles indicate the position of the La columns, showing that the Mn lattice is offset. Live acquisition time for the 64 × 64 spectrum image was ~30 s; field of view, 3.1 nm.

Fig. 2. (**A**) Individual EELS spectra from the series shown in Fig. 1. (**B**) The simultaneously recorded annular dark-field (ADF) image. The large red circles show that the La signal from Fig. 1A is correctly peaked where the ADF scattering is strongest. The small red dots indicate the spatial locations from which the EELS spectra were selected. Scale bar, 1 nm. (**C**) Background-subtracted and gain-corrected Ti L-edge spectra, plotted for a single line across the $SrTiO_3$ layer. The four fine-structure peaks corresponding to the unoccupied Ti 3d e_g and t_{2g} levels for the Ti L_3 and Ti L_2 edges are resolved.
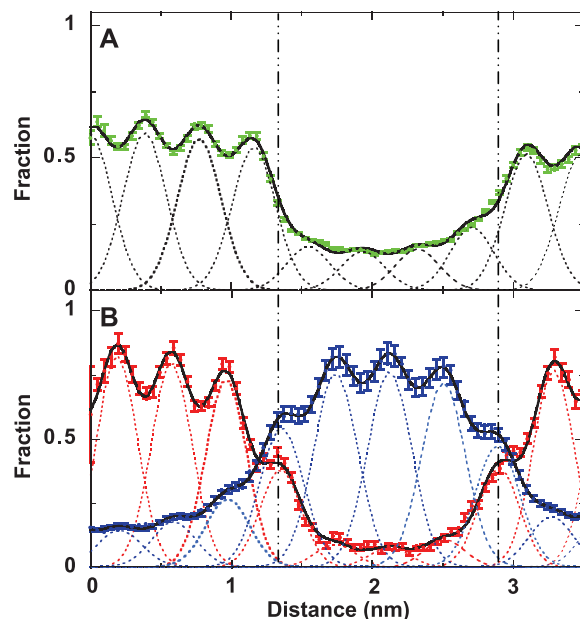
cannot change the shape of the spectrum, as PC2 does. Instead, whereas the Ti in the STO layer shows EELS fine structure typical of bulk SrTiO₃,

the Ti in the LSMO layer shows a strong damping of the crystal-field split levels, as is typical for local disorder such as binding to vacancies or other de-

fects (18, 19). Bonding changes on the oxygen sublattice are shown in fig. S3, again using a principal components analysis that is found to separate total concentration from chemical changes (11). Additional checks on common artifacts from beam spreading and delocalization are also given in (11).

Using one-component least-squares fits, we also built up concentration maps for La and Mn. These do not look significantly different from the simple summations of Fig. 1. The statistics for any given spectrum are relatively poor, but by averaging across the layer, the random fluctuations can be averaged out and we can obtain unbiased estimates of the random errors in the concentration measurement that we would not be able to obtain from a single line scan. Figure 4A shows that significant La has been incorporated in the nominal STO layer. The La profile at the left interface is abrupt, but at the right interface it is more gradual. There is also significant intermixing on the Mn-Ti sublattice at the last atomic plane in the STO layer (Fig. 4B). The chemical changes on the Ti edges show that these are different atoms, rather than probe tails from the neighboring layer (Fig. 3). (The presence of the core-level shift rules out the possibility that this is an inelastic tail from the STO layer, which would maintain the same shape.) The local concentration profiles are extracted by fitting a series of Gaussian peaks at each of the atomic columns. The width of the Gaussian reflects the averaging over random scan noise fluctuation between the 64 different image lines, rather than the actual and much smaller probe profile itself.

The experimental data show an asymmetry between A-site (La-Sr) and B-site (Mn-Ti) intermixing. Because the thin-film behavior of manganites shows a critical thickness behavior for conductivity, although the values vary (20–22), local compositional changes such as those seen here may have a key role to play.

We have demonstrated two-dimensional chemical imaging at the atomic scale, with simultaneous elemental identification and visualization of the local bonding states. The corrected optics allowed us to increase the convergence and collection angles. As a consequence, the elastic scattering artifacts that masked the chemical signal in earlier EELS work have been suppressed, and the image acquisition times were reduced by a factor of 10 to 100.

Fig. 3. Two-dimensional mapping of bonding details for the Ti and Mn 3d states, using only a single 0.5 eV–wide channel in the spectrum image (**A**) at the peak of the Ti L₂ e_g EELS edge, and (**B**) at the peak of the Mn L₃ edge, showing sufficient signal to form atomic-resolution images of the final-state density of states. To explore bonding variations across the multilayer, the Ti L spectrum image is rebinned to 32 × 32 pixels to improve the signal-to-noise ratio. (**C** and **D**) A principal components analysis gives two statistically significant components to the edge. The intensity scale of the second component is roughly 15% of that of the first component, reflecting the reduction in Ti concentration in the LSMO layer where this component is peaked. (**E**) The Ti L edge showing the crystal-field split Ti 3d e_g and t_{2g} empty states. The leftmost two peaks are transitions from the L₃ core level, and the rightmost two peaks are from the L₂ core level. The open and solid points are from single points (after rebinning) in the Ti-rich STO layer ("Ti in STO") and the Ti-poor LSMO layer ("Ti in LSMO"). The dotted lines are the fits from the first two principal components shown in (C) and (D). Field of view for all images, 3.1 nm.

Fig. 4. Line profiles averaged across the least-squares fit to the concentration maps of Fig. 1, corrected for the drift during acquisition. (**A**) The La M-edge concentration profile shows a small amount of La present inside the nominal SrTiO₃ layer and an asymmetry in intermixing between the sharp lower (left) and more gradual upper (right) interfaces. The black curve is a fit to a sum of Gaussian peaks fixed at the lattice sites (dashed), which gives an indication of the local La concentration partitioned by plane, showing the nominal SrTiO₃ is four unit cells thick in this region of the sample. (**B**) The Mn (red) and Ti (blue) profiles show a more symmetric intermixing at the two interfaces. The Ti displaced from these planes is spread throughout the LSMO layer, but the Mn in the STO layer is largely confined to these outermost planes. For all three curves, the colored error bars shown are the 95% confidence interval for the standard error of the mean (±2 SEM) calculated from the 64 different line profiles that make up each map.

References and Notes
1. J. C. H. Spence, J. Lynch, *Ultramicroscopy* **9**, 267 (1982).
2. P. E. Batson, *Nature* **366**, 727 (1993).
3. D. A. Muller, Y. Tzou, R. Raj, J. Silcox, *Nature* **366**, 725 (1993).
4. P. E. Batson, N. Dellby, O. L. Krivanek, *Nature* **418**, 617 (2002).
5. L. J. Allen, S. D. Findlay, A. R. Lupini, M. P. Oxley, S. J. Pennycook, *Phys. Rev. Lett.* **91**, 105503 (2003).
6. M. Bosman et al., *Phys. Rev. Lett.* **99**, 086102 (2007).
7. K. Kimoto et al., *Nature* **450**, 702 (2007).
8. O. L. Krivanek et al., *Ultramicroscopy*, 10.1016/j.ultramic.2007.07.010 (2007).
9. E. Okunishi, H. Sawada, Y. Kondo, M. Kersker, *Microsc. Microanal.* **12** (suppl. 2), 1150 (2006).
10. H. A. Brink, M. M. G. Barfels, R. P. Burgner, B. N. Edwards, *Ultramicroscopy* **96**, 367 (2003).
11. See supporting material on *Science* Online.

12. P. Stallknecht, H. Kohl, *Ultramicroscopy* **66**, 261 (1996).
13. E. C. Cosgriff, M. P. Oxley, L. J. Allen, S. J. Pennycook, *Ultramicroscopy* **102**, 317 (2005).
14. H. Kohl, H. Rose, *Adv. Imaging. Electron Phys.* **65**, 173 (1985).
15. D. A. Muller, J. Silcox, *Ultramicroscopy* **59**, 195 (1995).
16. R. F. Egerton, *Electron Energy Loss Spectroscopy in the Electron Microscope* (Plenum, New York, ed. 2, 1996).
17. P. Trebbia, N. Bonnet, *Ultramicroscopy* **34**, 165 (1990).
18. J. G. Chen, *Surf. Sci. Rep.* **30**, 1 (1997).
19. D. A. Muller, N. Nakagawa, A. Ohtomo, J. L. Grazul, H. Y. Hwang, *Nature* **430**, 657 (2004).
20. K. Dorr *et al.*, *J. Appl. Phys.* **89**, 6973 (2001).
21. X. Hong, A. Posadas, C. H. Ahn, *Appl. Phys. Lett.* **86**, 142501 (2005).
22. M. Izumi *et al.*, *Phys. Rev. B* **64**, 064429 (2001).
23. The instrument was developed under NSF grant DMR-9977547 with an additional contribution from Cornell University. In-kind contributions were made by Gatan Inc., Sandia National Laboratory, Pacific Northwest Laboratory, and Bell Laboratories. Supported by NSF Nanoscale Science and Engineering Initiative grant EEC-0117770 (D.A.M. and J.S.), NSF Materials Research Science and Engineering Center grant DMR-0520404 (L.F.K.), the TEPCO Research Foundation (H.Y.H.), and the Japan Society for the Promotion of Science (J.H.S.).

Extending Earthquakes' Reach Through Cascading

David Marsan* and Olivier Lengliné

Earthquakes, whatever their size, can trigger other earthquakes. Mainshocks cause aftershocks to occur, which in turn activate their own local aftershock sequences, resulting in a cascade of triggering that extends the reach of the initial mainshock. A long-lasting difficulty is to determine which earthquakes are connected, either directly or indirectly. Here we show that this causal structure can be found probabilistically, with no a priori model nor parameterization. Large regional earthquakes are found to have a short direct influence in comparison to the overall aftershock sequence duration. Relative to these large mainshocks, small earthquakes collectively have a greater effect on triggering. Hence, cascade triggering is a key component in earthquake interactions.

Earthquakes of all sizes, including after-shocks, are able to trigger their own aftershocks. The cascade of earthquake triggering causes the seismicity to develop complex, scale-invariant patterns. The cau-sality of "mainshock A triggered aftershock B," which appears so obvious if mainshock A happens to be large, must then be modified into a more subtle "mainshock A triggered C1, which triggered C2, ..., which triggered B." This has paramount consequences: The physical mechanism that causes direct trig-gering (static or dynamic stress changes, fluid flow, afterslip, etc.) cannot be studied by looking at aftershocks that were not directly triggered by the mainshock. More-over, if indirect triggering is important in the overall aftershock budget (*1–3*), then direct triggering must be confined to spatial ranges and times shorter than the size of the total

Laboratoire de Géophysique Interne et Tectonophysique, CNRS, Université de Savoie, 73376 Le Bourget du Lac, France.

*To whom correspondence should be addressed. E-mail: david.marsan@univ-savoie.fr

Fig. 1. Estimated rates and densities for California. (**A** and **B**) Bare kernels; (**C** and **D**) dressed kernels. The best power laws for the temporal rates $\lambda_t(t, m)$ and the best $[1 + (r/L)]^{-3}$ laws for the densities $\lambda_s(x, y, m)$ are shown as black dashed lines. The background temporal rate $\lambda_{0,t}$ [black horizontal line in (A) and (C)] is computed as $\sum_{i=1}^{N} w_{0,i}/T$. In (C) and (D), the dressed kernels (continuous lines) are compared to the bare ones (color dashed lines). The densities λ_s have been vertically shifted for clarity.